HHS Public Access

Author manuscript

Comput Biol Med. Author manuscript; available in PMC 2024 November 01.

Published in final edited form as:

Comput Biol Med. 2023 November ; 166: 107516. doi:10.1016/j.compbiomed.2023.107516.

Predicting the phase distribution during multi-channel transcranial alternating current stimulation *in silico* and *in vivo*

Sangjun Lee[1,†], **Sina Shirinpour**[1], **Ivan Alekseichuk**[1], **Nipun Perera**[1], **Gary Linn**[2,4], **Charles E. Schroeder**[2,3], **Arnaud Y. Falchier**[2,4], **Alexander Opitz**[1,†]

[1]Department of Biomedical Engineering, University of Minnesota, MN, USA

[2]Translational Neuroscience Lab Division, Center for Biomedical Imaging and Neuromodulation, The Nathan S. Kline Institute for Psychiatric Research, Orangeburg, NY, USA

[3]Departments of Neurological Surgery and Psychiatry, Columbia University College of Physicians and Surgeons, NY, USA

[4]Department of Psychiatry NYU Grossman School of Medicine, New York City, NY, USA

Abstract

Background: Transcranial alternating current stimulation (tACS) is a widely used noninvasive brain stimulation (NIBS) technique to affect neural activity. TACS experiments have been coupled with computational simulations to predict the electromagnetic fields within the brain. However, existing simulations are focused on the magnitude of the field. As the possibility of inducing the phase gradient in the brain using multiple tACS electrodes arises, a simulation framework is necessary to investigate and predict the phase gradient of electric fields during multi-channel tACS.

Objective: Here, we develop such a framework for phasor simulation using phasor algebra and evaluate its accuracy using *in vivo* recordings in monkeys.

Methods: We extract the phase and amplitude of electric fields from intracranial recordings in two monkeys during multi-channel tACS and compare them to those calculated by phasor analysis using finite element models.

Results: Our findings demonstrate that simulated phases correspond well to measured phases ($r = 0.9$). Further, we systematically evaluated the impact of accurate electrode placement on

[†]Corresponding Authors Information: Name: Alexander Opitz, aopitz@umn.edu, Address: 6-118 Nils Hasselmo Hall, 312 Church St SE, Minneapolis, MN, 55455, USA, Tel.: +1 612-624-1094; Name: Sangjun Lee, lee03936@umn.edu, Address: 6-112 Nils Hasselmo Hall, 312 Church St SE, Minneapolis, MN, 55455, USA.

Author Contributions

SL and AO conceived the study and designed the experiments. SS advised on data analysis. IA, GL, CES, and AYF acquired and preprocessed the data. IA and NP conducted the head modeling. AO supervised the study.

Declaration of Competing Interest

The authors declare that they have no competing interests.

modeling and data agreement. Finally, our framework can predict the amplitude distribution in measurements given calibrated tissues' conductivity.

Conclusions: Our validated general framework for simulating multi-phase, multi-electrode tACS provides a streamlined tool for principled planning of multi-channel tACS experiments.

Keywords

transcranial alternating current stimulation; phasor analysis; finite element method; nonhuman primate experiment

1. Introduction

Transcranial alternating current stimulation (tACS) is a noninvasive brain stimulation technique (NIBS) that aims to modulate brain oscillations in a frequency-specific manner by applying a weak external current via electrodes attached to the scalp [1]. Several studies have shown that tACS can improve various brain functions. However, researchers are still investigating the relationship between specific tACS parameters and behavioral outcomes. For instance, in healthy participants, theta tACS improved memory performance [2, 3]. Moreover, tACS can enhance motor-related excitability [4], long-term memory consolidation [5], and visual perception [6] by adjusting the stimulation frequency corresponding to the targeted brain function. Clinical trials have also shown promising results for tACS. It has been used to treat neurological and psychiatric symptoms such as depression, epilepsy, and schizophrenia [7–9], stroke rehabilitation [10], and Parkinson's disease [11].

TACS can entrain brain rhythms in a phase-specific manner by synchronizing intrinsic neural oscillations to its applied stimulation phase [12, 13]. To achieve this, tACS is traditionally applied by injecting two alternating currents with a 0° phase difference (in-phase) across distinct regions. [14]. It produces a standing wave electric field, which synchronizes brain areas with zero phase lag. In contrast, 180 ° (anti-phase) tACS is applied by two alternating currents with opposite phases known to be involved in the desynchronization of brain oscillations. Large-scale phase synchronization has been shown to play a crucial role in brain functions (e.g., working memory and long-term memory) [15, 16]. It is characterized by the phase synchrony of brain oscillations between distant brain regions (> 1 cm), with feedforward and feedback connections linking to different levels of the network in different brain regions [15]. Thus, tACS can be used to manipulate the phase alignment between distinct regions to modulate brain functions. For instance, previous studies demonstrated that in-phasic tACS over the frontal and parietal cortex for targeting the frontoparietal network improved working memory performance [17, 18]. On the contrary, anti-phasic tACS over the same regions deteriorated cognitive processes [19].

Using tACS input currents with defined phase shifts results in a traveling wave electric field. Electrophysiological traveling waves refer to time-lag neural oscillation patterns, characterized by a gradual phase shift of neural oscillations across the brain [20, 21]. Previous studies have shown that brain oscillations in low frequency bands propagate across the cortex in the form of traveling waves, especially during cognition [22, 23]. It has

been suggested that traveling waves are a key mechanism for explaining the transfer of information across cortical regions [22]. Alekseichuk et al. suggested that traveling wave tACS (twtACS) can entrain time-lagged brain oscillations across remote brain regions [24].

To predict and optimize the phasic electric field distribution during twtACS, it is necessary to develop and validate computational models. Computational simulations using the finite element method (FEM) have been well established to plan tACS experiments in human studies [25–27]. These simulation studies have mostly been focused on calculating the amplitude distribution of electric fields during tACS. A previous study demonstrated that the distribution of electric fields varies depending on whether in-phase or anti-phase tACS is used [28]. Our group previously suggested an analytical approach for calculating the electric field phase distribution during multi-channel tACS employing phasor algebra [24]. The phasor analysis allows determining the phase value inside the brain depending on the phase difference of the applied tACS currents. However, systematic validation and determination of the accuracy of our approach (hereafter referred to as “phasor simulation”) for predicting the phase of electric fields for tACS is still lacking.

Here we compare the phase distribution obtained from phasor simulation and *in vivo* intracranial recordings in two NHPs during multi-channel tACS to validate our computational modeling approach. Two active electrodes were placed on the scalp over the middle forehead and left occipital lobe. The return electrode was placed over the left temporal region. We extracted the phase and the amplitude of electric fields from intracranial recordings in two NHPs under various stimulation phase conditions. Then, we conducted the phasor simulation using head models to calculate phasic electric fields under the same conditions as in recordings, followed by a comparison of the measured and simulated results. In addition, we evaluate the effect of a small displacement of the return electrode on the phase distribution in simulations, which is essential for the formation of a phase gradient. As FEM simulations have a tendency to overestimate the electric field amplitude [29], we also optimize the electrical conductivity of NHP tissues to minimize the error between measured and simulated amplitudes. Our results demonstrated that simulated phases show a high correlation with *in vivo* recorded phases in both monkeys. Further calibration of the electrical conductivity of the tissues improved the correspondence between the simulated and measured amplitudes, in line with a previous study [30]. Importantly, our findings expand conventional amplitude-based computational simulation of tACS towards phase-amplitude simulation. Finally, our framework allows the prediction of the phase distribution generated by tACS for ad hoc optimization in future studies.

2. Materials and methods

2.1. In vivo experiments in nonhuman primates

2.1.1. Nonhuman primates—All procedures were approved by the Institutional Animal Care and Use Committee of the Nathan Kline Institute for Psychiatric Research. Two NHPs were utilized in experiments. Monkey 1 is a female capuchin monkey (11 years old, and 2.9 kg) whereas monkey 2 is a female rhesus macaque (6 years old, 4.8 kg). In all monkeys, three stereo-EEG (sEEG) (Ad-Tech Medical Instruments Corporation, Racine, Wisconsin, USA) electrodes with 5 mm spacing between electrode contacts were

implanted through an entry point in the left occipital cortex. Electrodes were aligned in anterior-posterior direction. One sEEG electrode had an endpoint in the frontal cortex (12 contacts, the other in the medial prefrontal cortex (10 contacts), and another in the anterior hippocampus (10 contacts).

2.1.2. Transcranial alternating current stimulation—tACS protocols and *in vivo* recordings were carried out according to the previous study [24]. tACS using the multi-channel Starstim system (Neuroelectrics, Barcelona, Spain) was applied to the monkeys with two active electrodes placed on the scalp above the forehead (anterior electrode) and over the left occipital lobe (posterior electrode), respectively. Both monkeys were anesthetized during tACS. The return electrode was attached to the scalp over the temporal region. All the electrodes were round, with a radius of 10 mm. While injecting the alternating current with a fixed phase of 0° from the anterior electrode, we injected the alternating current with the phase varying from 0° to 360° in a step of 15° for the posterior electrode, with the amplitude (peak-to-zero) fixed to 0.1 mA at a frequency of 10 Hz. Through the preliminary experiments, it was confirmed that the amplitude of the current was sufficient to generate the 10 Hz oscillation at sEEG contacts. The current at the return electrode is set so that the sum of all electrode currents always sums to zero. This led to 25 different stimulation conditions with different phase differences between the two active electrodes. For each condition, the stimulation duration and ramping up/down time were 30 s and 5 s, respectively.

2.1.3. Data acquisition and analysis—While injecting tACS, electric potentials in sEEG electrodes were acquired at a sampling rate of 5 kHz using a BrainAmp MR plus amplifier (Brain Products) for monkey 1 and a Cortech NeurOne Tesla amplifier (Cortech Solution, Wilmington, NC) for monkey 2. The raw data were band-pass filtered at cut-off frequencies of 5 Hz and 20 Hz using a 4th-order zero-phase Butterworth filter [24], then downsampled to 1 kHz using MATLAB 2021b (MathWorks) and the Fieldtrip toolbox [31]. The relatively broad bandpass with forward-reverse in time was used to prevent phase distortion and signal amplitude loss. With the elimination of the 5 s ramping up/down period, 30 s of electric potentials for 25 stimulation conditions were extracted and rescaled to the electric potential when the current of 1 mA was assumed to be injected [24]. Then, we examined preprocessed data and post-implanted MR images to assess for signal contamination and abnormal sEEG contact placement. The contacts outside the gray matter (GM) and white matter (WM) were removed for both monkeys. For monkey 1, three contacts were excluded and interpolated from neighboring contacts. For monkey 2, one sEEG electrode was entirely omitted due to low signal quality. In addition, the front two contacts of the sEEG electrode implanted over the hippocampus were positioned on the boundary between GM and CSF, and substantially twisted relative to the other contacts. Due to the possibility of inaccurate calculations of electric fields resulting from misalignment among contacts, these two contacts were excluded from the analysis. After removing the contacts, a total of 28 contacts from three sEEG electrodes (A1, A2, and A3) and a total of 19 contacts from two sEEG electrodes (B1 and B2) were utilized to calculate the phase (see Fig. 1A). Note that sEEG electrodes were located along the anterior-posterior direction with the frontal cortex (A1 and B1), the medial prefrontal cortex (A2), and the anterior hippocampus (A3 and B2) as the endpoints. Also, three stimulation conditions (0°, 180°,

and 360°) were excluded from further analysis because they cannot generate phase-gradient electric fields (similar to traditional tACS). The 0° condition (which is the same as 360 ° condition) and 180 ° condition can only produce the phase distribution with 0° and 180° inside the brain. Note that the aim of this study is to investigate how accurately phasor simulation can predict a tACS-induced phase gradient to manipulate time-lag brain oscillations across brain regions. Thus, 22 stimulation conditions were considered for data analysis. A visual inspection of the data was performed to confirm the removal of several noise sources, including DC offset, high frequency components, and power line interference, by the bandpass filter. The filtering process successfully provided a prominent sine wave oscillating at a frequency of 10 Hz. Then, electric fields were calculated using the numerical gradient of measured electric potentials (zero-padded to 2^{15} samples) along contacts for each sEEG electrode. As all sEEG electrodes were aligned in the anterior-posterior direction, we were able to quantify the electric field in the anterior-posterior direction at each contact. Using the Fast Fourier Transform (FFT), we extracted the phase φ and amplitude $|E|$ of electric fields at each contact for the maximum frequency (which was equal to the stimulation frequency, 10 Hz) and centered the phase values along each sEEG electrode between $-\pi/2$ and $\pi/2$ following unwrapping them [32].

2.2. Computational simulation for the phase analysis using head models

2.2.1. Realistic finite element model—Realistic head models of the monkey head were created using T1-weighted magnetic resonance (MR) images (pre-implanted MR images) acquired before sEEG electrodes were implanted. We extracted the GM and WM masks using a modified Human Connectome Project pipeline for non-human primates [33]. This pipeline requires Freesurfer [34] and FSL [35]. In addition, we performed manual modification for GM and WM masks using ITK-SNAP to include anatomical information that is not captured by automatic segmentation [36]. The masks for the scalp, skull, cerebrospinal fluid (CSF), and eyes were constructed by manual segmentation. FSL's FLIRT package was used to register MRI from native space to the Freesurfer space [37, 38], and then Gmsh was used to generate a volumetric head model from tissue masks [39] (see Fig. 1B). We then determined the precise location of sEEG electrodes used in *in vivo* experiments on the volumetric head models for both monkeys by matching post-implanted MR images to pre-implanted MR images using FSL.

2.2.2. Electric field simulation—For each monkey model, two active electrodes and the return electrode, with a diameter of 10 mm and a thickness of 5 mm, were attached to the scalp. The location of tACS electrodes was identical to that of *in vivo* experiments. The following conductivity values were used for phasor simulation: 0.465 S/m for the scalp, 0.5 S/m for the eyes, 0.01 S/m for the skull, 1.654 S/m for the CSF, 0.275 S/m for the GM, and 0.126 S/m for the WM. We calculated electric fields inside the brain by solving the Laplace equation given by $-\nabla \cdot (\sigma \nabla V) = 0$, where σ represents the electrical conductivity and V represents the electrical potential. To solve this problem, Dirichlet boundary condition was set to fixed potentials imposed on one of the active electrodes (anterior electrode) and the return electrode, with a fixed potential of 1 V applied to the upper side of the active electrode and 0 V applied to the upper side of the return electrode. Then, the finite element solver GetDP [40] implemented in SimNIBS [41] was used by employing the Galerkin

method to calculate the electric field distribution inside the brain [42]. The electric field in the entire domain was rescaled by the ratio of the injection current to be 1 mA. The same process was applied for the other active electrode (the posterior electrode) and the return electrode, resulting in two independent electric field distributions, $\mathbf{E_1}$ (anterior electrode – return electrode) and $\mathbf{E_2}$ (posterior electrode – return electrode).

2.2.3. Phasor simulation—Then, the direction of electric fields was captured in the anterior – posterior direction for each sEEG electrode. Considering the desired d-direction of electric fields for a specific sEEG electrode, resultant electric fields in this direction were defined as $E_1^d = \mathbf{E}_1 \cdot d$ and $E_2^d = \mathbf{E}_2 \cdot d$. Then, we employed a phasor analysis to the resultant electric field distributions obtained from the previous step. Assuming that alternating currents at a specific frequency with phases of θ_1 and θ_2 were injected through the anterior and posterior electrodes, respectively, the phasic electric fields of P_1 and P_2 at any given location were determined as follows:

$$P_1 = E_1^d cos\theta_1 + j\left(E_1^d sin\theta_1\right) \tag{1}$$

$$P_2 = E_2^d cos\theta_2 + j\left(E_2^d sin\theta_2\right) \tag{2}$$

Then, the electric field P at any point generated from three-electrode tACS can be determined by the superposition of the two electric fields P_1 and P_2 as

$$P = P_1 + P_2 = \left(E_1^d cos\theta_1 + E_2^d cos\theta_2\right) + j\left(E_1^d sin\theta_1 + E_2^d sin\theta_2\right) \tag{3}$$

From the electric field P, we can estimate the amplitude $\left|\widehat{E}\right|$ and the phase $\widehat{\varphi}$ of the electric field P as follows:

$$\left|\widehat{E}\right| = \sqrt{P_1^2 + P_2^2} \tag{4}$$

$$\widehat{\varphi} = tan^{-1}\left(\frac{E_1^d sin\theta_1 + E_2^d sin\theta_2}{E_1^d cos\theta_1 + \mathrm{E}_2^d cos\theta_2}\right) \tag{5}$$

With this step, we can determine the phase and amplitude in the anterior-posterior direction for each contact of a specific sEEG electrode, followed by unwrapping of the phase angles and centering them between $-\pi/2$ and $\pi/2$. Given that d-direction was different among sEEG electrodes, we repeated the abovementioned steps for each sEEG electrode for each

monkey to derive the accurate phase and amplitude at each electrode contact considering the directionality of electric fields as in *in vivo* experiments.

2.3. Data analysis

2.3.1. Comparison between measured and simulated results—We visualized the distribution of the phase and amplitude of the directional electric fields obtained from the measurements and simulations for 22 stimulation conditions. Also, the polar graph with normalized amplitude for each stimulation condition was illustrated for each sEEG electrode. Then, we quantified the similarity between measured and simulated phase values by the circular correlation coefficient using the circular statistics toolbox [43], as follows:

$$R = \frac{\sum_{i=1}^{N} \left[sin(\varphi_i - \overline{\varphi}) sin\left(\widehat{\varphi}_i - \overline{\widehat{\varphi}}\right) \right]}{\sqrt{\sum_{i=1}^{N} sin(\varphi_i - \overline{\varphi}_i)^2} \sqrt{\sum_{i=1}^{N} sin\left(\widehat{\varphi}_i - \overline{\widehat{\varphi}}_i\right)^2}} \tag{6}$$

where N is the total number of contacts. φ_i and $\widehat{\varphi}_i$ represent the phase of the i-th contacts in measurements and simulations, respectively. $\overline{\varphi}$ and $\overline{\widehat{\varphi}}$ represent the mean values for these phases. For a comparison of the amplitude, we used Pearson's correlation to determine the correlation coefficient between measured and simulated amplitudes. Since we already accounted for the directionality of each sEEG electrode, R values were calculated using all contacts.

2.3.2. Effects of the return electrode placements—Once the direction of electric fields is determined to be anterior to posterior, the placement of the return electrode plays an important role in the characterization of electric fields. Thus, a small displacement of the return electrode in head models can cause a mismatch with the actual measurements. To explore this, the return electrode location was shifted in a 7-by-7 grid in the anterior-posterior (7 steps) and inferior-superior (7 steps) directions, with a step size of 5 mm (50% of the electrode radius), relative to the original location of the return electrode (which is referred to as the center of the grid), resulting in a total of 49 displacement points on the scalp. Certain points were excluded because they overlapped with the left ear, where the electrode could not be attached. For each displacement point, the simulated and measured results were compared.

2.3.3. Optimization of electrical conductivity—In the current study, the electrical conductivity of human tissues was applied to the monkey models. This may cause a disparity between simulation and experiment, specifically for the amplitude of electric fields. To overcome this gap, we optimized the electrical conductivity by comparing measured and simulated amplitudes obtained from all stimulation conditions to find the best match. We employed the same optimization problem as in the previous study [30], as follows:

$$\sigma_{\text{optimal}} = \underset{\sigma}{\operatorname{argmin}} f(\sigma), \quad \text{where } f(\sigma) = \frac{1}{M}\sum_{i=1}^{M}\left|\,|E|_i - \left|\hat{E}\right|_i(\sigma)\right|^2 \tag{7}$$

where $|E|_i$ is the measured amplitude at the contact i and $\left|\hat{E}\right|_i(\sigma)$ represents the simulated amplitude depending on the estimated electrical conductivity σ. M is the total number corresponding to the number of sEEG contacts × stimulation conditions. The problem was solved using a pattern search algorithm [44]. This algorithm is suitable for finding the solution that has the lowest error value on discontinuous and nondifferential functions. The conductivity value of the original phasor analysis was used as the initial conductivity. σ was iteratively updated within a given range specified in the previous study [30] to minimize the cost function $f(\sigma)$. The optimal electrical conductivity σ_{optimal} was determined for both monkeys. In the optimization process, we only considered the electrical conductivity of four tissues, including the scalp, skull, GM, and WM, as a variable, while the electrical conductivity of other liquid-filled tissues (CSF and eyes) is assumed to be a constant. We then investigated whether employing the optimal conductivity in simulations may effectively lessen the disagreement with *in vivo* recordings by calculating the absolute error for each stimulation condition as

$$\text{Error} = \frac{1}{N}\sum_{i=1}^{N}\left|\,|E|_i - \left|\hat{E}\right|_i\right| \tag{7}$$

where N is the total number of sEEG electrode contacts. $|E|_i$ is the measured amplitude at the contact i, and $\left|\hat{E}\right|_i$ is the simulated amplitude when applying either initial or optimal conductivity. With either initial or optimal conductivity, we can derive the errors for two conductivity cases for the 22 different stimulation conditions, followed by a non-parametric statistical comparison of these two errors using the Wilcoxon signed-rank test.

3. Results

3.1. Comparison between simulated and measured results

Figure 2 shows the comparison between the simulated and measured phase distributions and polar graph with normalized amplitude for sEEG electrode A2 for four representative stimulation conditions (45°, 135°, 225°, and 315°) in monkey 1. Those conditions were chosen for the purpose of demonstrating the distinctive features of twtACS in relation to the phase gradient. For stimulation conditions less than 180 ° , the simulation results show a phase distribution with a greater phase value in the anterior part of the sEEG electrodes, and vice versa (see Fig. 2A). In addition, the farther the stimulation condition is from 180°, the greater the phase difference between electrodes. These findings are consistent with our previous study [24]. Similarly, fig. 2B shows the phase gradient among contacts is well

represented in the computational simulation relative to *in vivo* experiments. The other polar graphs for the other sEEG electrodes for both monkeys are shown in Supplementary Figures. 1–5.

We confirmed that the simulation can predict the phase distribution for both monkeys (Fig. 3A and B) across all stimulation conditions. Note that the phase and amplitude distributions at sEEG electrodes for the other stimulation conditions are illustrated in Supplementary Figures. 6 and 7. To quantify the similarity, we calculated the correlation coefficient (R) for all stimulation conditions. For instance, we illustrate a correlation graph for the 45° stimulation condition, showing simulated phases are in good agreement with measured phases (Fig. 3C and D, left panel). Likewise, under most stimulation conditions, the R value is close to 0.9, with the mean R values of 0.89 ± 0.10 and 0.90 ± 0.16 for monkey 1 and monkey 2, respectively (Fig. 3C and D, right panel). Figure 4 shows the comparison between the simulated and measured amplitude distributions. Amplitude distributions in all sEEG electrodes are quite similar in both the simulation and experiment; however, the amplitude is comparably greater in the simulations for both monkeys (Fig. 4A and B). This is also evident in the correlation graph with higher values on the axis representing simulations (Fig. 4C and D). Nevertheless, the simulation accurately predicts the distribution of the amplitudes for the *in vivo* experiments with the mean R values of 0.81 ± 0.06 and 0.75 ± 0.12 for monkey 1 and monkey 2, respectively.

3.2. Change in the correlation depending on the return electrode placement

Next, we examined how a small displacement of the return electrode in head models affects the correlation between simulated and measured outcomes. For both monkeys, the mean correlation coefficient of the phase and amplitude for all stimulation conditions was highest close to the original location (Figs. 5A and C). However, the correlations continuously declined as the return electrode was moved farther from the center. For monkey 1, the correlation values did not markedly change when moving the return electrode in the inferior-superior direction, although a considerable decrease in both correlation values of the phase and amplitude was observed in the anterior-posterior direction as shown in Fig. 5B. In monkey 2, the correlation values decreased regardless of the displacement direction as the return electrode was attached far from the center (Fig. 5D). Furthermore, in both monkeys, the correlation values of amplitudes are considerably more sensitive to the return electrode shifts than the phase correlations. The correlation values tend to be higher within the range between −5 mm and 5 mm from the center, implying that the minimum radius of 5 mm (50% of the electrode radius) for the return electrode displacement is most optimal for an accurate simulation to capture phasic electric field distribution during a tACS experiment.

3.3. Effects of employing optimal electrical conductivity

Given a comparable difference in the amplitude between simulations and experiments, we individually calibrated the electrical conductivities in head models to optimize the similarity in amplitudes. The correlation values are either consistent with or slightly higher than the standard conductivity values used in computational modeling previously [45] for the 22 stimulation conditions when employing the optimal conductivity, whereas the amplitude itself was decreased for both monkeys in comparison to those employing the

initial conductivity (Figs. 6A and B). We confirmed that the mean absolute errors in the case of the optimal conductivity (0.05 ± 0.01 for monkey 1 and 0.10 ± 0.02 for monkey 2) were significantly smaller than those in the case of the initial conductivity of 0.26 ± 0.01 and 0.27 ± 0.02, respectively ($p < 0.05$ for both monkeys) (See Fig. 6C). This indicates that an optimization process can be used to determine the tissue's electrical properties, thereby overcoming the difference of the amplitude between the computational simulation and *in vivo* experiments. The optimal conductivity values are listed in Supplementary Table. 1.

4. Discussion

This is the first study to validate the accuracy of phasor simulation for tACS with *in vivo* measurements. Our study has three main findings: i) the phasor simulation using head models achieves an accurate prediction of the phase distribution inside the brain for multi-channel tACS; ii) the simulation precisely predicts the phase in *in vivo* experiments only when the return electrode is positioned within a small radius from the actual location; and iii) the tendency of the simulated electric field amplitude distribution follows the measured amplitude, while an overestimation in the electric field amplitude can be calibrated by optimizing the electrical conductivity. Notably, 22 experimental stimulation conditions for tACS in two monkeys were used for our analysis. We further developed individual head models that can adequately capture the anatomical structure. Consequently, our findings provide solid and clear evidence that phasor analysis in the head model can capture the properties of tACS electric fields from phase-shifted inputs.

Our findings show that the phasor simulation accurately predicts the phase gradient along sEEG electrodes as observed in intracranial recordings (Supplementary Figures 6A and 7A). We confirmed that a phase shift between the anterior and posterior electrodes is visible in simulations when injecting the currents with a phase difference higher than 180° [24]. As depicted in Fig. 3, under most stimulation conditions, the correlation values between simulated and measured phases were between 0.9 and 0.95, with a maximum of 0.94 and 0.98, for monkey 1 and monkey 2, respectively (Supplementary Figures 8A and 10A). Still, some caution should be made when interpreting our findings. First, some differences exist in the phase value at each sEEG contact between simulations and measurements. This might be due to several factors, such as limited data quality of *in vivo* recordings at some contacts and the misestimation of electric fields due to uncertainty in the electrical properties of brain tissues. However, for traveling waves the phase difference (or phase gradient) across targeted regions is more important than the accurate phase estimation at a single location in the brain. From this perspective, our phase estimation can accurately capture the phase gradient in *in vivo* measurements. Thus, our findings provide important evidence that computational models based on phasor algebra can accurately estimate the phase of recorded electric fields extracted from the complex fourier values in FFT.

The location of the stimulation electrodes, especially the return electrode, is crucial for an accurate estimation of traveling wave electric fields. This is because the electric field direction will be determined as in-phasic or anti-phasic based on the location of the return electrode when the directionality of the electric field is determined (Figure 1A). Our results show that the return electrode has to be placed very precisely (< 5 mm distance) to properly

estimate the phasic information of electric fields as in *in vivo* recordings. This is in line with a previous study suggesting that the minimal displacement required to ensure the accuracy of simulations in human head models was less than 10 mm [29]. Furthermore, the location of the return electrode is related to the direction of the electric field. Figure 5 shows that correlation values are more sensitive to the anterior-posterior displacement of the return electrode. Especially, the correlation values for the amplitude dropped dramatically when the return electrode was attached to the posterior part of the head. This could be explained by a previous finding indicating that electric fields are predominantly shunted through the scalp when the electrodes are close together [46, 47]. Therefore, the precise location of the return electrode while considering the direction of the traveling wave to be manipulated by tACS is essential for a reliable prediction.

The phasor simulation also estimated the spatial distribution of electric field amplitude inside the brain at a similar level to previous validation studies [30, 32, 41] (Supplementary Figures. 6B and 7B). However, the simulated amplitude itself was considerably higher than the measured one. This is due to a systematical overestimation in head models when using a well-known electrical property measured in ex-vivo conditions [29, 30, 48]. For instance, the maximum amplitudes in simulations were about 0.8 V/m and 1.2 V/m for monkey 1 and monkey 2, respectively, whereas those in measurements were about 0.4 V/m and 0.8 V/m (Supplementary Figures. 9A and 11A). This difference can be significantly reduced by using optimal conductivity values in simulations. Despite this, we must be cautious in interpreting optimization results. The aim of the optimization was to minimize the error between simulated and measured amplitudes. Thus, it is more appropriate to regard the role of optimal conductivity as a calibration [30].

Although the simulation results had a high correlation with the measurement data, there are some numerical differences, resulting in a non-uniform phase gradient (see Fig. 3 and Supplementary Figure. 12). This may originate from simulation errors due to the absence of tissue anisotropy in the model. WM anisotropy does not markedly affect the electric field distribution over cortical regions but alters the electric field distribution inside the brain [49]. Imperfect segmentation of the boundary between WM and GM may also disrupt the uniform phase gradient as observed in measurements. Nevertheless, our model captures the observed pattern of electric field (Supplementary Figure. 12). Furthermore, we did not consider sEEG electrodes, wires, and skull opening in the models. The modeling of sEEG electrodes and wiring would have minor effect on electric field because the metal implants generally act as insulators in tACS-induced electric fields [50]. For skull opening, it can alter the electric field distribution over cortical regions, in relation to the shunting effect [51]. However, it would have a minor impact on changes in phase gradient inside the brain, as indicated by a strong correlation between simulated and measured results. Nevertheless, future work should investigate the effects of invasive implants and operations on the simulation results.

NHP models have been commonly used to explore biophysical effects of tACS due to their similarity of anatomical structures to humans [13, 32, 52]. Therefore, we can extend our understanding of our results to human participants. We studied the biophysics of tACS, thus we intentionally used stimulation intensities below what is necessary for neuromodulation [53] but sufficient to characterize the electric field phase. The efficacy of tACS with

tolerable current intensity (1–2 mA) used in humans remains controversial due to the lack of currents delivered to the brain [51]. Future studies on humans should adjust the stimulation dose to satisfy a minimum electric field for manipulating traveling waves in the brain. Furthermore, there is inter-subject variability in the outcomes of tACS [54]. This could be addressed with personalized electrode placement [55]. Based on our findings, it will be important to precisely place the return electrode in human experiments. This can be achieved, for example, by digitizing the coordinates of electrodes on the scalp corresponding to those in the human head model using a 3D digitizer in clinical experiments [56]. In addition, the phase values at sEEG contacts are not markedly different between the cases employing initial and optimal conductivities. This indicates that the phase distribution is quite robust to the change of tissue conductivities (Supplementary Figures 8 - 11). Our results indicate that ohmic properties dominantly affect the amplitude of oscillations, not phasic information. Thus, a consistent phase distribution would be expected among participants as long as the stimulation phase condition is the same.

Further investigation would be required to examine the phase distribution throughout the cortical regions, as traveling waves propagate along the overlying cortex. This can be accomplished in *in vivo* experiments using electrocorticography (ECoG), as demonstrated in a previous study [21]. The following stage would be to investigate whether twtACS can manipulate ongoing traveling waves associated with brain functions, such as cognition [21, 57], sensory processing [58], and visual processing [59]. Our framework can predict the phase gradient. The next step would be to develop a multi-channel tACS optimization that can determine optimal electrode conditions (e.g., the phase and amplitude of injecting currents, electrode position) to generate the desired phase gradient over targeted regions.

In summary, we validated the accuracy of the phasor simulation in two monkeys via *in vivo* measurements. Our findings provide clear evidence that the phasor simulation can accurately estimate the phase distribution in the form of traveling waves as well as the spatial distribution of the amplitude inside the brain during multi-channel tACS. An additional calibration through the optimization of the electrical conductivity was required to better match predicted and measured electric field amplitudes. Our study lays the foundation for optimized multi-channel tACS that can manipulate ongoing brain oscillations in a phase-specific manner.

Supplementary Material

Refer to Web version on PubMed Central for supplementary material.

Acknowledgments

This research was supported in part by NIH (1RF1MH124909-01) and in part by a grant of the Korea Health Technology R&D Project through the Korea Health Industry Development Institute (KHIDI), funded by the Ministry of Health & Welfare, Republic of Korea (grant number: HI21C1234).

Data Availability

Please contact the corresponding author (aopitz@umn.edu) for data requests.

References

1. Wischnewski M, Alekseichuk I, and Opitz A, Neurocognitive, physiological, and biophysical effects of transcranial alternating current stimulation. Trends in Cognitive Sciences, 2022.
2. Alekseichuk I, et al. , Spatial working memory in humans depends on theta and high gamma synchronization in the prefrontal cortex. Current biology, 2016. 26(12): p. 1513–1521. [PubMed: 27238283]
3. Alekseichuk I, et al. , Model-driven neuromodulation of the right posterior region promotes encoding of long-term memories. Brain Stimulation, 2020. 13(2): p. 474–483. [PubMed: 31882373]
4. Schilberg L, et al. , Phase of beta-frequency tACS over primary motor cortex modulates corticospinal excitability. cortex, 2018. 103: p. 142–152. [PubMed: 29635161]
5. Ketz N, et al. , Closed-loop slow-wave tACS improves sleep-dependent long-term memory generalization by modulating endogenous oscillations. Journal of Neuroscience, 2018. 38(33): p. 7314–7326. [PubMed: 30037830]
6. Salamanca-Giron RF, et al. , Enhancing visual motion discrimination by desynchronizing bifocal oscillatory activity. NeuroImage, 2021. 240: p. 118299. [PubMed: 34171500]
7. Ahn S, et al. , Targeting reduced neural oscillations in patients with schizophrenia by transcranial alternating current stimulation. Neuroimage, 2019. 186: p. 126–136. [PubMed: 30367952]
8. Haller N, et al. , Gamma transcranial alternating current stimulation improves mood and cognition in patients with major depression. Journal of psychiatric research, 2020. 130: p. 31–34. [PubMed: 32771678]
9. San-Juan D, et al. , A pilot randomized controlled clinical trial of Transcranial Alternating Current Stimulation in patients with multifocal pharmaco-resistant epilepsy. Epilepsy & Behavior, 2022. 130: p. 108676. [PubMed: 35366528]
10. Naros G and Gharabaghi A, Physiological and behavioral effects of β-tACS on brain self-regulation in chronic stroke. Brain stimulation, 2017. 10(2): p. 251–259. [PubMed: 27965067]
11. Guerra A, et al. , Driving motor cortex oscillations modulates bradykinesia in Parkinson's disease. Brain, 2022. 145(1): p. 224–236. [PubMed: 34245244]
12. Krause MR, et al. , Transcranial alternating current stimulation entrains single-neuron activity in the primate brain. Proceedings of the National Academy of Sciences, 2019. 116(12): p. 5747–5755.
13. Johnson L, et al. , Dose-dependent effects of transcranial alternating current stimulation on spike timing in awake nonhuman primates. Science advances, 2020. 6(36): p. eaaz2747. [PubMed: 32917605]
14. Polanía R, et al. , The importance of timing in segregated theta phase-coupling for cognitive performance. Current Biology, 2012. 22(14): p. 1314–1318. [PubMed: 22683259]
15. Varela F, et al. , The brainweb: phase synchronization and large-scale integration. Nature reviews neuroscience, 2001. 2(4): p. 229–239. [PubMed: 11283746]
16. Fell J and Axmacher N, The role of phase synchronization in memory processes. Nature reviews neuroscience, 2011. 12(2): p. 105–118. [PubMed: 21248789]
17. Violante IR, et al. , Externally induced frontoparietal synchronization modulates network dynamics and enhances working memory performance. elife, 2017. 6: p. e22001. [PubMed: 28288700]
18. Draaisma L, et al. , Targeting the frontoparietal network using bifocal transcranial alternating current stimulation during a motor sequence learning task in healthy older adults. Brain Stimulation, 2022. 15(4): p. 968–979. [PubMed: 35792318]
19. Takeuchi N, Terui Y, and Izumi S-I, Oscillatory entrainment of neural activity between inferior frontoparietal cortices alters imitation performance. Neuropsychologia, 2021. 150: p. 107702. [PubMed: 33276036]
20. Bolt T, et al. , A parsimonious description of global functional brain organization in three spatiotemporal patterns. Nature Neuroscience, 2022. 25(8): p. 1093–1103. [PubMed: 35902649]
21. Zhang H, et al. , Theta and alpha oscillations are traveling waves in the human neocortex. Neuron, 2018. 98(6): p. 1269–1281. e4. [PubMed: 29887341]

22. Muller L, et al. , Cortical travelling waves: mechanisms and computational principles. Nature Reviews Neuroscience, 2018. 19(5): p. 255–268. [PubMed: 29563572]
23. Halgren M, et al. , The generation and propagation of the human alpha rhythm. Proceedings of the National Academy of Sciences, 2019. 116(47): p. 23772–23782.
24. Alekseichuk I, et al. , Electric field dynamics in the brain during multi-electrode transcranial electric stimulation. Nature communications, 2019. 10(1): p. 2573.
25. Baltus A, et al. , Optimized auditory transcranial alternating current stimulation improves individual auditory temporal resolution. Brain stimulation, 2018. 11(1): p. 118–124. [PubMed: 29079460]
26. Rufener KS, et al. , Transcranial electrical stimulation improves phoneme processing in developmental dyslexia. Brain stimulation, 2019. 12(4): p. 930–937. [PubMed: 30826318]
27. Klírová M, et al. , Modulating inhibitory control processes using individualized high definition theta transcranial alternating current stimulation (HD θ-tACS) of the anterior cingulate and medial prefrontal cortex. Frontiers in Systems Neuroscience, 2021. 15: p. 611507. [PubMed: 33859554]
28. Saturnino GB, et al. , How to target inter-regional phase synchronization with dual-site transcranial alternating current stimulation. Neuroimage, 2017. 163: p. 68–80. [PubMed: 28919407]
29. Opitz A, et al. , On the importance of precise electrode placement for targeted transcranial electric stimulation. Neuroimage, 2018. 181: p. 560–567. [PubMed: 30010008]
30. Huang Y, et al. , Measurements and models of electric fields in the in vivo human brain during transcranial electric stimulation. Elife, 2017. 6: p. e18834. [PubMed: 28169833]
31. Oostenveld R, et al. , FieldTrip: open source software for advanced analysis of MEG, EEG, and invasive electrophysiological data. Computational intelligence and neuroscience, 2011. 2011: p. 1–9. [PubMed: 21837235]
32. Opitz A, et al. , Spatiotemporal structure of intracranial electric fields induced by transcranial electric stimulation in humans and nonhuman primates. Scientific reports, 2016. 6(1): p. 1–11. [PubMed: 28442746]
33. Fair DA, et al. , Correction of respiratory artifacts in MRI head motion estimates. Neuroimage, 2020. 208: p. 116400. [PubMed: 31778819]
34. Fischl B, FreeSurfer. Neuroimage, 2012. 62(2): p. 774–781. [PubMed: 22248573]
35. Jenkinson M, et al. , Fsl. Neuroimage, 2012. 62(2): p. 782–790. [PubMed: 21979382]
36. Yushkevich PA, et al. , User-guided 3D active contour segmentation of anatomical structures: significantly improved efficiency and reliability. Neuroimage, 2006. 31(3): p. 1116–1128. [PubMed: 16545965]
37. Jenkinson M, et al. , Improved optimization for the robust and accurate linear registration and motion correction of brain images. Neuroimage, 2002. 17(2): p. 825–841. [PubMed: 12377157]
38. Jenkinson M and Smith S, A global optimisation method for robust affine registration of brain images. Medical image analysis, 2001. 5(2): p. 143–156. [PubMed: 11516708]
39. Geuzaine C and Remacle JF, Gmsh: A 3-D finite element mesh generator with built-in pre- and post-processing facilities. International journal for numerical methods in engineering, 2009. 79(11): p. 1309–1331.
40. Dular P, et al. , A general environment for the treatment of discrete problems and its application to the finite element method. IEEE Transactions on Magnetics, 1998. 34(5): p. 3395–3398.
41. Puonti O, et al. , Value and limitations of intracranial recordings for validating electric field modeling for transcranial brain stimulation. Neuroimage, 2020. 208: p. 116431. [PubMed: 31816421]
42. Opitz A, et al. , Determinants of the electric field during transcranial direct current stimulation. Neuroimage, 2015. 109: p. 140–150. [PubMed: 25613437]
43. Jammalamadaka SR and SenGupta A, Topics in circular statistics Vol. 5. 2001: world scientific.
44. Audet C and Dennis JE Jr, Analysis of generalized pattern searches. SIAM Journal on optimization, 2002. 13(3): p. 889–903.
45. Alekseichuk I, et al. , Comparative modeling of transcranial magnetic and electric stimulation in mouse, monkey, and human. Neuroimage, 2019. 194: p. 136–148. [PubMed: 30910725]

46. Faria P, Hallett M, and Miranda PC, A finite element analysis of the effect of electrode area and inter-electrode distance on the spatial distribution of the current density in tDCS. Journal of neural engineering, 2011. 8(6): p. 066017. [PubMed: 22086257]
47. Seibt O, et al. , The pursuit of DLPFC: non-neuronavigated methods to target the left dorsolateral pre-frontal cortex with symmetric bicephalic transcranial direct current stimulation (tDCS). Brain stimulation, 2015. 8(3): p. 590–602. [PubMed: 25862601]
48. Opitz A, et al. , Limitations of ex vivo measurements for in vivo neuroscience. Proceedings of the National Academy of Sciences, 2017. 114(20): p. 5243–5246.
49. Shahid SS, et al. , The value and cost of complexity in predictive modelling: role of tissue anisotropic conductivity and fibre tracts in neuromodulation. Journal of neural engineering, 2014. 11(3): p. 036002. [PubMed: 24737098]
50. Mercadal B, et al. , Modeling implanted metals in electrical stimulation applications. Journal of Neural Engineering, 2022. 19(2): p. 026003.
51. Vöröslakos M, et al. , Direct effects of transcranial electric stimulation on brain circuits in rats and humans. Nature communications, 2018. 9(1): p. 483.
52. Huang WA, et al. , Transcranial alternating current stimulation entrains alpha oscillations by preferential phase synchronization of fast-spiking cortical neurons to stimulation waveform. Nature communications, 2021. 12(1): p. 3151.
53. Alekseichuk I, Wischnewski M, and Opitz A, A minimum effective dose for (transcranial) alternating current stimulation. Brain Stimulation: Basic, Translational, and Clinical Research in Neuromodulation, 2022. 15(5): p. 1221–1222.
54. Laakso I, et al. , Inter-subject variability in electric fields of motor cortical tDCS. Brain stimulation, 2015. 8(5): p. 906–913. [PubMed: 26026283]
55. van Bueren NE, et al. , Personalized brain stimulation for effective neurointervention across participants. PLoS computational biology, 2021. 17(9): p. e1008886. [PubMed: 34499639]
56. Nieminen AE, et al. , Accuracy and precision of navigated transcranial magnetic stimulation. Journal of Neural Engineering, 2022. 19(6): p. 066037.
57. Kleen JK, et al. , Bidirectional propagation of low frequency oscillations over the human hippocampal surface. Nature communications, 2021. 12(1): p. 2764.
58. Lozano-Soldevilla D and VanRullen R, The hidden spatial dimension of alpha: 10-Hz perceptual echoes propagate as periodic traveling waves in the human brain. Cell reports, 2019. 26(2): p. 374–380. e4. [PubMed: 30625320]
59. Alamia A, et al. , Distinct roles of forward and backward alpha-band waves in spatial visual attention. Elife, 2023. 12: p. e85035. [PubMed: 36876909]

Highlights

- The phase distribution obtained from phasor simulation during multi-channel tACS is compared with *in vivo* measurements recorded in monkeys.
- Our findings show that simulated phases correspond well to measured phases.
- Our framework for phasor simulation provides the opportunity to predict the phasic information of electric fields in the brain during traveling wave tACS..

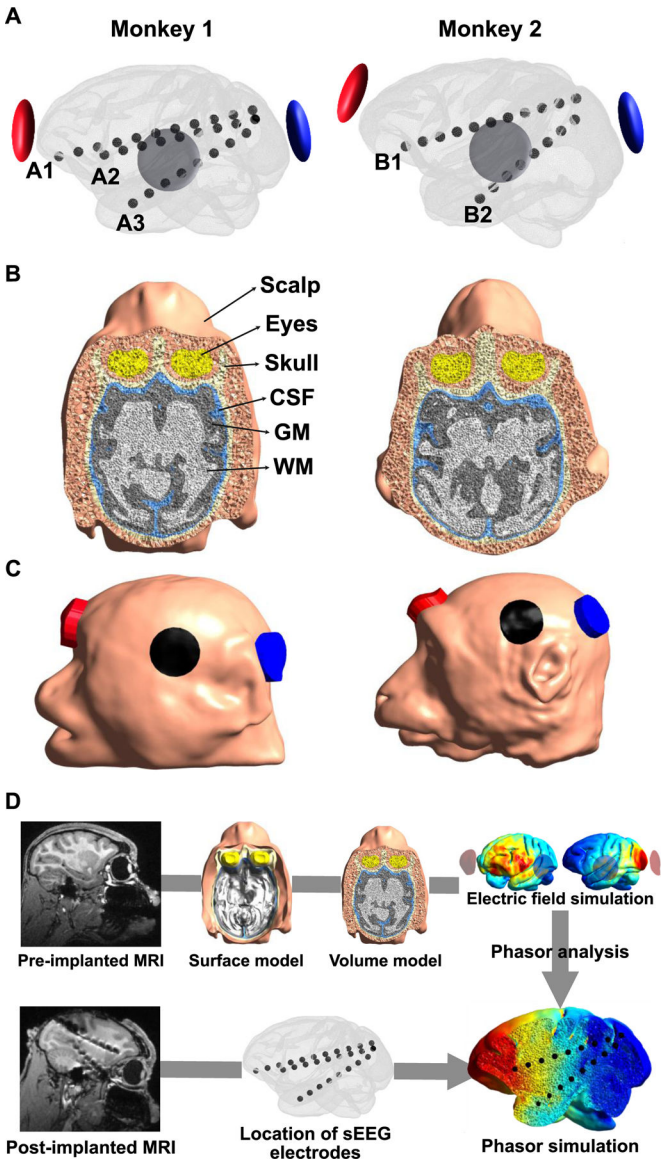

Figure. 1.

A) Illustration of the location of sEEG electrodes and tACS electrodes. Three and two sEEG electrodes were used for further data analysis for monkey 1 and monkey 2, respectively. The sEEG electrodes were located along the anterior-posterior direction with the frontal cortex (A1 and B1), the medial prefrontal cortex (A2), and the anterior hippocampus (A3 and B2) as the endpoints, respectively. B) Illustration of volumetric head models, including the scalp, skull, CSF, GM, WM, and eyes. C) Location of tACS electrodes in head models. The red and blue represent the active electrodes (anterior and posterior electrodes, respectively), and the black represents the return electrode. The alternating current with a consistent phase of 0° was applied through the anterior electrode (red), while the alternating current with a phase varying from 0° to 360° was applied through the posterior electrode (blue). The amplitude of the current was fixed to 0.1 mA. D) The pipeline for the phasor simulation.

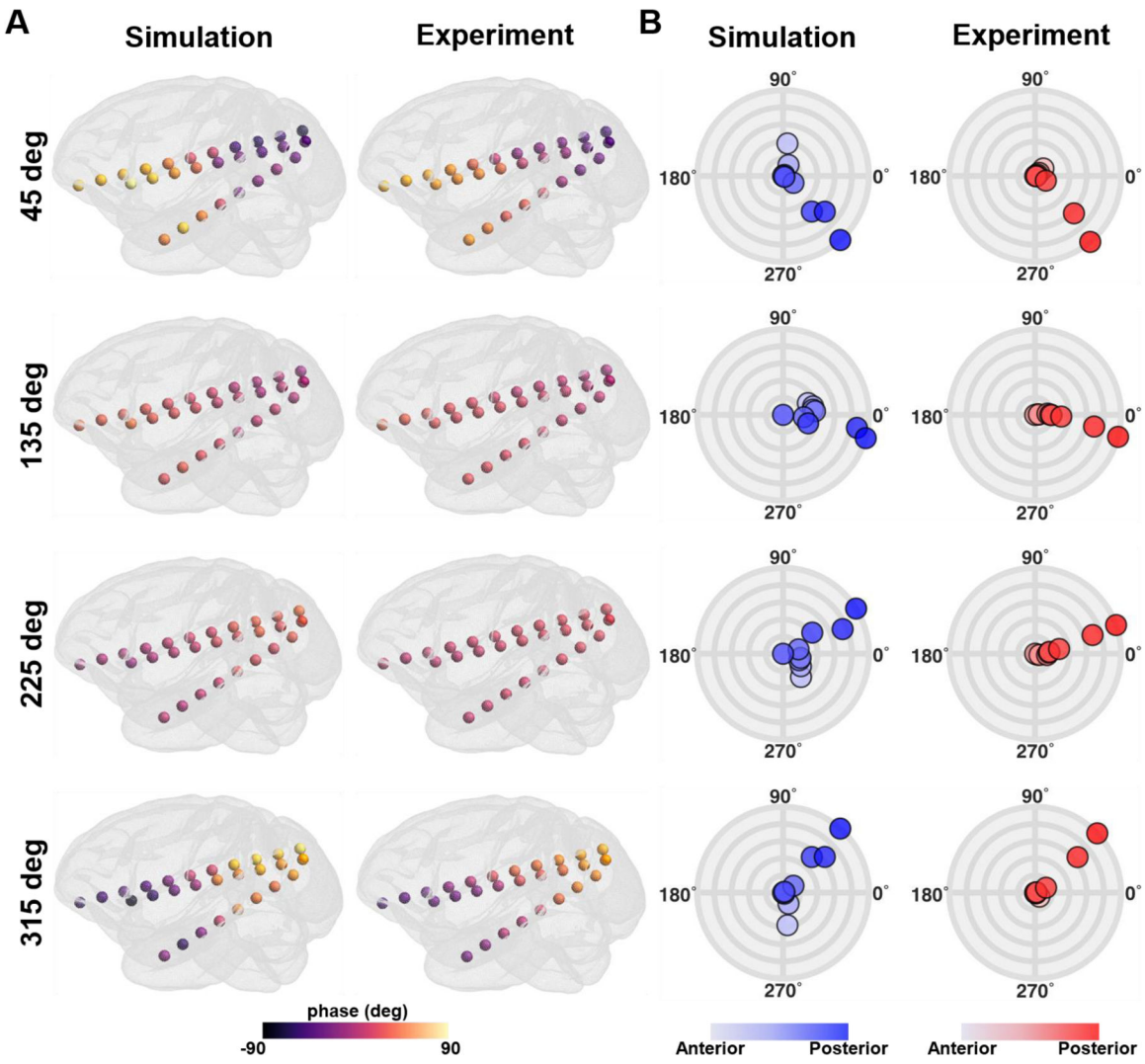

Figure. 2.

Comparison between simulations and *in vivo* measurements for four representative stimulation conditions (45°, 135°, 225°, and 315°). A) The phase distribution at all sEEG electrodes in monkey 1. B) The polar graph with the phase and the normalized amplitude at all contacts of sEEG electrode A2 in monkey 1. Colored circles represent individual contacts in the sEEG electrode, with a gradual color gradient along the anterior-posterior direction. The outermost circular line in the polar graph represents the normalized amplitude of 1, with an interval of 0.2 between circular lines.

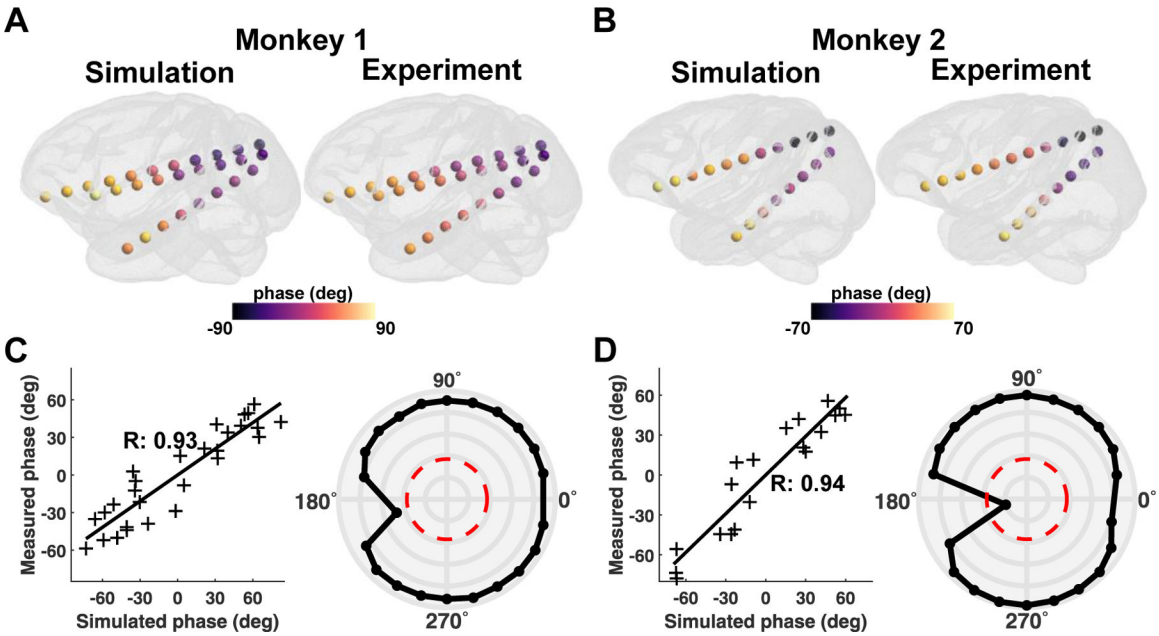

Figure. 3.

Comparison between simulations and *in vivo* measurements for the phase. A, B) Illustration of the phase distribution at all sEEG electrodes during 45° stimulation condition for both monkeys. C, D) The example correlation between simulated and measured phases for 45° stimulation condition (left panel). The polar graph depicts the correlation values between measurements and simulations for each stimulation condition for both monkeys (right panel). The red line in the polar graph denotes the significance level of $p = 0.05$, while the outermost circular line in the polar graph represents a correlation value of 1, with an interval of 0.2 between circular lines.

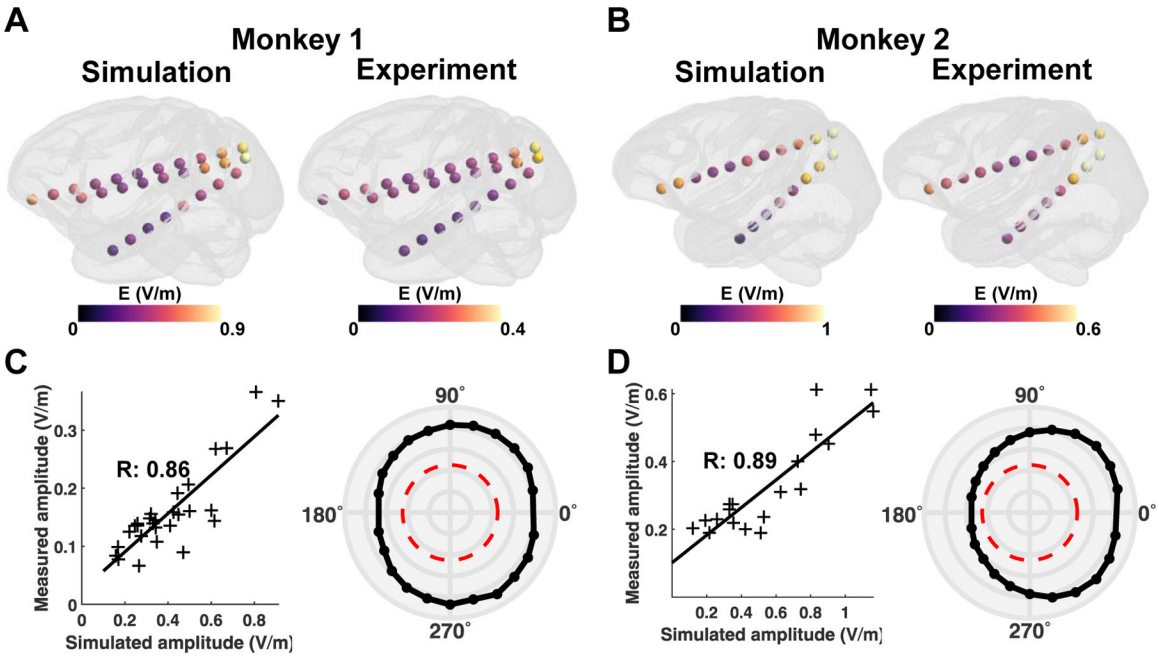

Figure. 4.

Comparison between simulations and *in vivo* measurements for the amplitude. A, B) Illustration of the amplitude distribution at all sEEG electrodes during the 45° stimulation condition for both monkeys. C, D) The example correlation between simulated and measured amplitudes for 45° stimulation condition (left panel). The polar graph depicts the correlation values for each stimulation condition for both monkeys (right panel). The red line in the polar graph denotes the significance level of $p = 0.05$, while the outermost circular line in the polar graph represents a correlation value of 1, with an interval of 0.2 between circular lines.

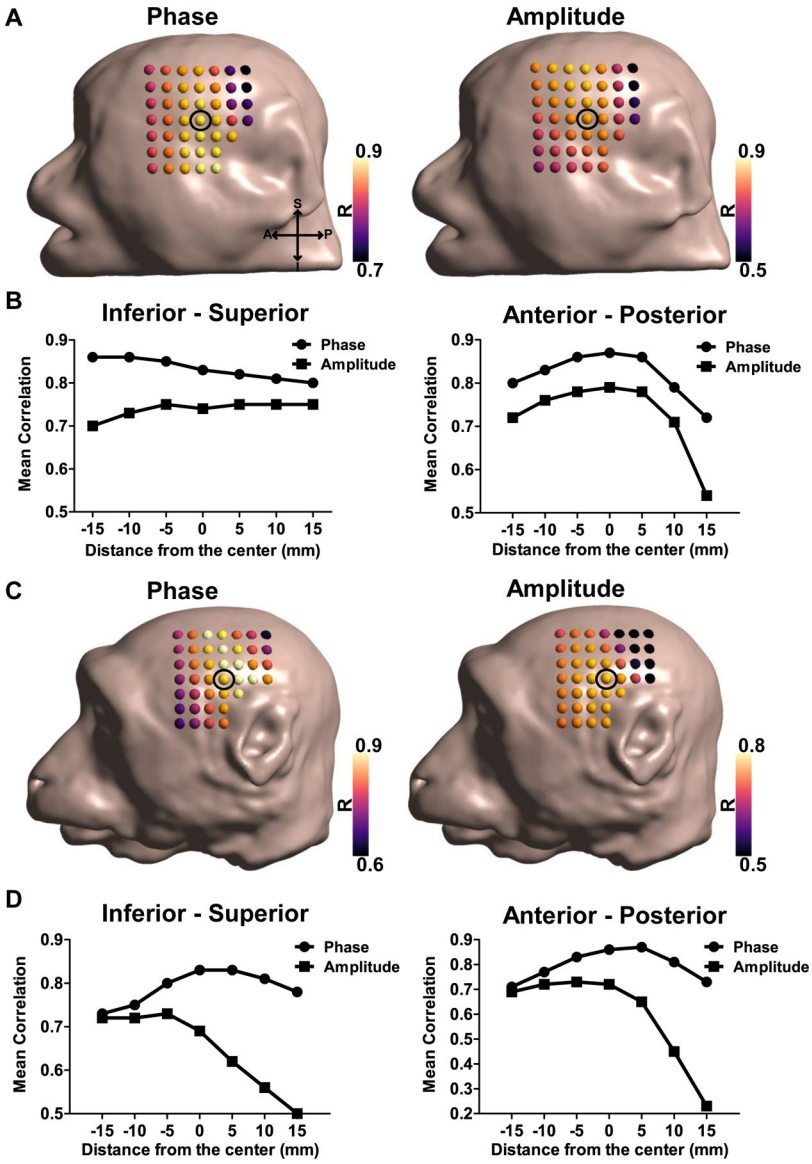

Figure. 5.

Effects of a small displacement of the return electrode. The mean correlation values between simulated and measured results (phase and amplitude) for all stimulation conditions as the return electrode was moved in steps of 5 mm for A) monkey 1 and C) monkey 2. The black circle indicates the center of the displacement (the original position of the return electrode), while the dots in head models represent the return electrode locations. B, D) Mean correlation values for the phase and amplitude with a distance from the center along the inferior-superior (left panel) and anterior-posterior directions (right panel).

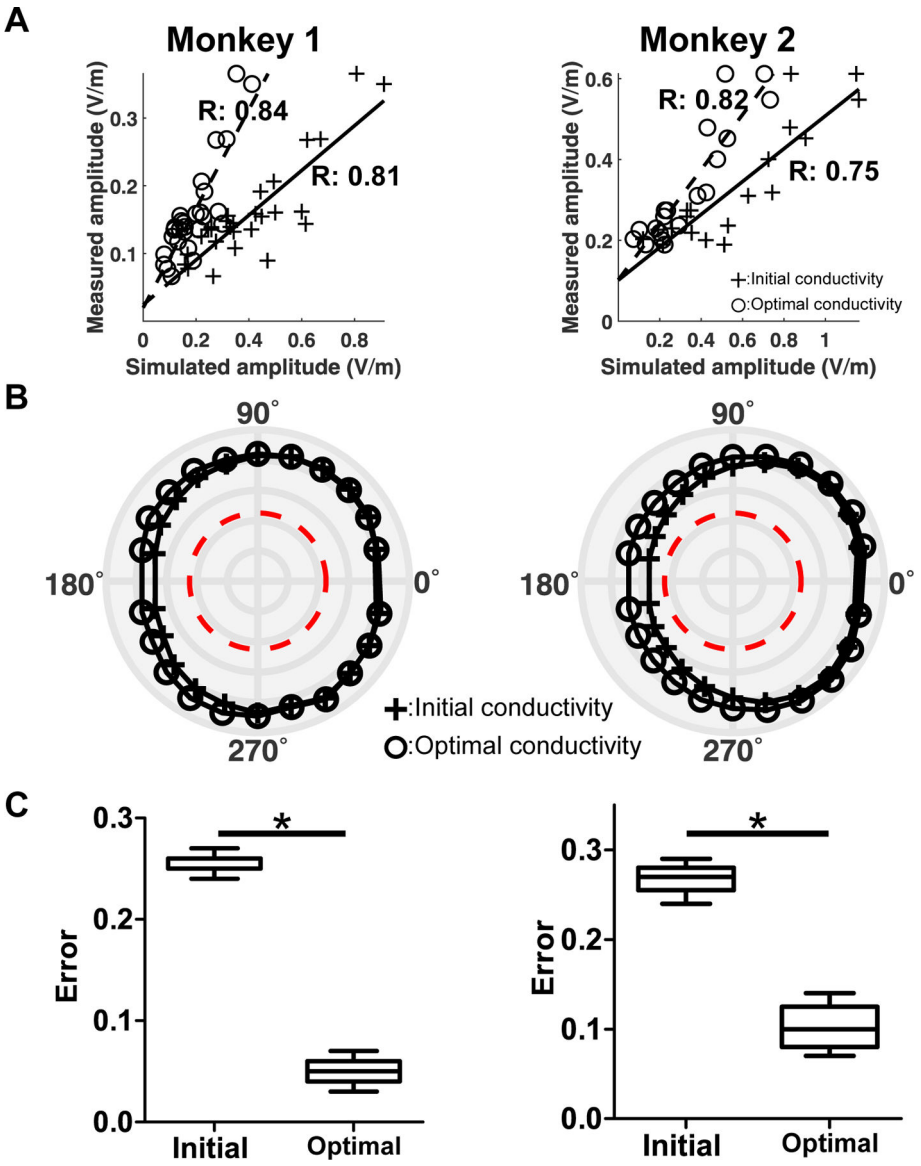

Figure. 6.

Effects of employing the optimal conductivity in the computational simulations for monkey 1 (left column) and monkey 2 (right column). A) Comparison of the correlation of the amplitude with that obtained by applying the optimal conductivity. The cross symbols with the solid line are associated with the simulated amplitude obtained by applying the initial conductivity, and the circle symbols with the dotted line are associated with the simulated amplitude when applying the optimal conductivity. B) Correlation values for all 22 stimulation conditions when either applying initial or optimal conductivities. The red line represents the significance level of $p = 0.05$. C) The absolute amplitude error for all stimulation conditions ($n = 22$) between measured and simulated amplitudes obtained by either applying the initial or optimal conductivities ($*p < 0.05$). The 'Initial' represents the error between the measured amplitude and simulated amplitude when applying the initial

conductivity, while the ‘Optimal’ represents the error between the measure amplitude and simulated amplitude when applying the optimal conductivity.